

18 **Breaking structure sensitivity in CO₂ hydrogenation by tuning**
19 **metal–oxide interfaces in supported cobalt nanoparticles**

20 **Alexander Parastaev¹, Valery Muravev¹, Elisabet Huertas Osta¹, Tobias F. Kimpel¹,**
21 **Jérôme F.M. Simons¹, Arno J.F. van Hoof¹, Evgeny Uslamin¹, Long Zhang¹, Job J.C.**
22 **Struijs¹, Dudari B. Burueva^{2,3}, Ekaterina V. Pokochueva^{2,3}, Kirill V. Kovtunov^{2†}, Igor V.**
23 **Koptuyug², Ignacio J. Villar-Garcia⁴, Carlos Escudero⁴, Thomas Altantzis⁵, Pei Liu⁶,**
24 **Armand Béché⁶, Sara Bals⁶, Nikolay Kosinov¹, Emiel J. M. Hensen^{1,*}**

25 ¹*Inorganic Materials and Catalysis, Eindhoven University of Technology, 5600 MB Eindhoven,*
26 *The Netherlands*

27 ²*Laboratory of Magnetic Resonance Microimaging, International Tomography Center, SB*
28 *RAS, 630090 Novosibirsk, Russia*

29 ³*Novosibirsk State University, 630090 Novosibirsk, Russia*

30 ⁴*ALBA Synchrotron Light Source, 08290 Cerdanyola del Vallès, Barcelona, Spain*

31 ⁵*ELCAT, University of Antwerp, 2610 Wilrijk, Belgium*

32 ⁶*EMAT, University of Antwerp, 2020 Antwerp, Belgium*

33 *†Deceased author*

34 **Corresponding author: e.j.m.hensen@tue.nl*

35

36

37 **Abstract**

38 A high dispersion of the active metal phase of transition metals on oxide supports is important
39 when designing efficient heterogeneous catalysts. Besides nanoparticles, clusters and even
40 single metal atoms can be attractive for a wide range of reactions. However, many industrially-
41 relevant reactions suffer from structure sensitivity, where reducing the size of the metal particles
42 below a certain size substantially lowers the catalytic performance. A case in point is the low
43 activity of small cobalt nanoparticles in the hydrogenation of CO and CO₂. Herein we show
44 how engineering catalytic sites at the metal–oxide interface in ceria-zirconia-supported cobalt
45 can overcome this structure sensitivity. Few-atom cobalt clusters dispersed on 3 nm cobalt(II)-
46 oxide particles stabilized by ceria-zirconia yield a highly active CO₂ methanation catalyst with
47 a specific activity higher than those of larger particles under the same conditions.

48 **Main**

49 Supported metals are an important class of industrial heterogeneous catalysts. Increasing the
50 metal dispersion is a common strategy to maximize the amount of exposed metal atoms^{1,2}.
51 However, this approach does not always lead to better catalysts, because the intrinsic activity
52 (*i.e.*, per exposed metal atom) can depend strongly on metal dispersion. Especially,
53 nanoparticles smaller than 10 nm exhibit a strong size dependence of the contributions of
54 surface terrace, corner, edge, and step-edge sites, where differences in coordination numbers
55 and surface topology may lead to substantial difference in the intrinsic activity. This
56 phenomenon is broadly known as structure sensitivity^{3,4} and underlies the particle size
57 dependence of important industrial reactions such as ammonia synthesis^{5,6}, Fischer-Tropsch
58 synthesis⁷, CO₂ methanation⁸, methanol synthesis⁹, ethylene hydrogenation¹⁰ and (dry)
59 methane reforming¹¹. Many studies have been devoted to understand the nature of structure
60 sensitivity, in particular for CO and CO₂ hydrogenation¹². For instance, the optimum size of
61 cobalt particles for CO hydrogenation in the Fischer-Tropsch reaction is around 6 – 8 nm^{7,13},
62 which implies that a large amount of the metal is not directly involved in the catalytic reaction.
63 A possible approach to overcome conventional structure sensitivity could be the design of
64 catalysts containing additional active sites other than metal nanoparticles, *i.e.*, metal–oxide
65 interfacial sites^{14,15} or non-innocent supports¹⁶. Also, the presence of highly dispersed ionic
66 species instead of metallic particles can lead to superior catalytic performance². The promise of
67 such approaches can be highlighted by recent examples for CO oxidation¹⁷ and the water-gas
68 shift reaction^{18,19}. For CO and CO₂ hydrogenation, only a few studies hinted at the involvement
69 of relatively large (partially) oxidized supported and unsupported cobalt nanoparticles^{20–23}. As
70 CO₂ hydrogenation is expected to be a key technology for storing surplus renewable energy in
71 chemical energy carriers²⁴, there is a need to develop more efficient catalysts.

72 In this work, we show that the temperature of reductive pretreatment prior reaction can be used
73 to tune the nature of the interfaces between cobalt and the metal oxides present in the
74 cobalt/ceria-zirconia catalysts. In this way, we can overcome the limitations imposed by
75 conventional structure sensitivity and obtain catalysts with a much higher cobalt utilization
76 efficiency in CO₂ hydrogenation resulting in an unusually high catalytic activity of small (3
77 nm) cobalt/cobalt (II) oxide nanoparticles.

78

79

80 **Results**

81 **Structure sensitivity**

82 Recently, we demonstrated that the Co – O – Ce interface between large cobalt particles and
83 ceria-zirconia is active in CO₂ methanation¹⁴. Here, we constructed metal–oxide interfacial
84 active sites in cobalt-ceria-zirconia catalysts (CoCZ) using cobalt oxide nanoparticles with
85 similar reduction behavior in the 2.5 – 20 nm range (see **Supplementary Notes 1 and 2**). To
86 tune the nature of the interfacial metal–oxide active sites, the reduction degree of CoCZ
87 catalysts was adjusted by varying the reduction temperature in the 225 – 500 °C range.

88 **Fig. 1** summarizes the catalytic results for different reduction temperatures and nanoparticle
89 sizes. Cobalt catalysts completely reduced at 500 °C exhibit the strong size-activity dependence
90 (**Fig. 1a**, Volcano plot 1) that is typical for CO₂ hydrogenation catalyzed by metallic cobalt⁷
91 (**Supplementary Note 5**). At this relatively high reduction temperature, the catalyst with the
92 smallest cobalt particles (1% CoCZ, **Fig. 1b**) displayed a low activity in CO₂ methanation with
93 CO as the main reaction product. The highest activity was observed for the 5% CoCZ sample
94 containing nanoparticles with sizes in the 7–9 nm range and with CH₄ as the main reaction
95 product. To exclude the possibility that restructuring of cobalt nanoparticles or strong metal–
96 support interaction (SMSI) led to a lower activity of small cobalt nanoparticles due to
97 encapsulation of the active phase by the reducible ceria support²⁵, we carried out *in situ*
98 scanning transmission electron microscopy electron energy loss spectroscopy (STEM-EELS)
99 experiments (**Supplementary Note 4**). **Fig. 1d** underlines the absence of ceria on the surface
100 of cobalt nanoparticles upon reduction of 1% CoCZ catalyst at 500 °C. CO chemisorption, XPS,
101 H₂ – D₂ exchange and UV-Vis and IR spectroscopy data confirm the absence of SMSI in CoCZ
102 catalysts (**Supplementary Note 3**).

103 Changing the reduction temperature in the range of 275 – 500 °C did not have a substantial
104 effect on the catalytic performance of CoCZ catalysts containing relatively large Co
105 nanoparticles (> 7 nm). The catalysts containing small nanoparticles, on the other hand,
106 demonstrated different behavior after reduction at lower temperatures (**Fig. 1a**, Volcano plot
107 2). The catalytic activity of 1% CoCZ notably increased when lowering the reduction
108 temperature with a pronounced maximum at 300 °C (referred to as 1Co300). 1Co300 displayed
109 a ten-fold higher activity than 1Co500. When normalized to the amount of cobalt, 1Co300
110 presents a much higher catalytic activity for the Sabatier reaction than other cobalt and nickel
111 catalysts described in the literature (**Supplementary Note 5**).

112 To summarize, **Fig. 1a** shows two types of volcano plots. The first one as a function of particle
113 size (volcano plot 1) exhibits an optimum around 7 – 9 nm, which is exemplary of conventional
114 structure sensitivity observed for CO_x hydrogenation using cobalt catalysts⁷. The second
115 volcano plot has an optimum at intermediate reduction temperature of 300 °C for low-loaded
116 cobalt on ceria-zirconia, leading to an unusually high methanation activity (volcano plot 2). To
117 understand this unexpected finding, we investigated the structure of small (1% CoCZ) and large
118 (10% CoCZ, **Fig. 1c**) cobalt nanoparticles reduced at different temperatures by a combination
119 of advanced (*in situ*) spectroscopy and microscopy.

120 **Nature of active sites of partially reduced catalysts**

121 Typically, catalytic CO and CO₂ hydrogenation has been associated with metallic nanoparticles.
122 Temperature-programmed reduction profiles and *quasi in situ* XPS analysis show that the cobalt
123 particles in 1Co500 and 10Co500 catalysts are fully metallic (**Supplementary Notes 2 and 6**).
124 When reduction is carried out at lower temperature, surface analysis by lab-based *quasi in situ*
125 XPS shows that the cobalt nanoparticles in 10Co300 are composed of a mixture of CoO and Co
126 metal (**Supplementary Figure 33**). The small nanoparticles in 1Co275 (**Supplementary**
127 **Figure 33**) and 1Co300 (**Fig. 2a**) are composed only of CoO. However, as we found that these
128 samples strongly chemisorb CO at 30 °C (**Supplementary Notes 1 and 3**), we surmised the
129 presence of reduced cobalt. To verify this, we exploited the much higher surface sensitivity of
130 synchrotron-based *in situ* NAP-XPS. **Fig. 2b** demonstrates that the very surface of 1Co300
131 contains metallic cobalt. Deconvolution of the Co 2p_{3/2} XPS spectrum shows that the surface
132 of this sample contains approximately equal amounts of Co⁰ and Co²⁺. The presence of a
133 mixture of Co⁰ and Co²⁺ was further confirmed by CO IR spectra recorded at low temperature
134 (**Fig. 2c, Supplementary Note 7**).

135 To elucidate the nature of the metallic Co sites, we analyzed CO IR spectra of 1% CoCZ after
136 reduction at different temperatures (**Fig. 2d**). An unusually narrow carbonyl band at 2025 –
137 2040 cm^{-1} was observed for 1Co275 and 1Co300. The sharpness of this feature in comparison
138 to CO adsorbed on cobalt metal nanoparticles is a strong indication for the presence of very
139 small and uniform metallic clusters or even single atoms of cobalt^{26–28}. It is yet more likely that
140 the catalyst contains small cobalt clusters, because of the presence of additional relatively
141 narrow bands at $\sim 1940 \text{ cm}^{-1}$ and $\sim 1870 \text{ cm}^{-1}$ related to multi-bonded carbonyls²⁹. The observed
142 IR features are in line with stretching vibrational frequencies computed by density functional
143 theory for small metallic Co_n clusters placed on the CoO(111) surface (**Supplementary Note**
144 **8**). The full width at half maximum (FWHM) of the linear carbonyl band in 1Co300 (14 cm^{-1})
145 is slightly higher than the value of 10 cm^{-1} for 1Co275 (**Fig. 2d**). This difference can indicate
146 an increasing size of the metallic cobalt clusters after reduction at $300 \text{ }^\circ\text{C}$. The CO IR spectrum
147 for 1Co500 demonstrates that this sample contains predominantly metallic cobalt particles, as
148 also indicated by the XPS results. It is well established that the carbonyl band on extended
149 metallic cobalt surfaces shifts to higher wavenumbers with increasing CO coverage due to
150 lateral interactions between the adsorbed CO molecules²⁹. The 1% CoCZ catalyst reduced at
151 lower temperatures exhibits a different IR response with respect to CO coverage (**Fig. 2e**). The
152 blue shifts for 1Co275 and 1Co300 of respectively 4 cm^{-1} and 12 cm^{-1} are much smaller than
153 the $>20 \text{ cm}^{-1}$ shifts observed for the 1Co350 and 1Co500 catalysts. Such a difference further
154 underpins the conclusion that 1Co275 and 1Co300 (**Fig. 2f**) contain very small metallic cobalt
155 clusters, unlike 1Co350 and 1Co500 samples featuring predominantly metallic surfaces. The
156 small metallic cobalt clusters cannot be obtained by mild reduction of CoCZ samples with a
157 larger cobalt particle size (**Fig. 2g, Supplementary Note 7**). The presence of Co metal clusters
158 on small CoO particles is likely the reason behind the unusual catalytic activity of these
159 materials.

160

161 **Origin of unconventional structure sensitivity**

162 To unravel the underlying phenomena of structure sensitivity in CO_2 hydrogenation, we
163 compared the activation of CO_2 and H_2 reactants and CO as a reaction intermediate on the
164 surface of CoCZ catalysts. CO_2 can be activated at the interface of metal particles and a
165 reducible support containing oxygen vacancies, leading to the formation of formate species³⁰.
166 In a catalytic cycle, an oxygen vacancy in the reducible support would be healed during CO_2
167 dissociation and later regenerated by H_2 . It can be expected that the catalytic performance

168 within the formate pathway increases with the number of interfacial sites and the rate of oxygen
169 vacancy regeneration³⁰. Formate species are formed on the surface of all CoCZ samples upon
170 steady-state exposure to the reaction mixture (**Fig. 3a**), which is indicated by bands at 1577
171 cm^{-1} , 1365 cm^{-1} [31], and 2845 cm^{-1} [32,33]. The negative band at 2115 cm^{-1} implies that the ceria
172 support is partially re-oxidized by CO_2 [31]. We further studied the redox dynamics in the CoCZ
173 catalysts by following the transient switches between H_2 and CO_2/H_2 mixture (**Fig. 3b**). The
174 facile reduction-oxidation of the CZ support is confirmed by the reversible behavior of surface
175 hydroxyl species³⁴ and subsurface oxygen vacancies during these experiments. The observed
176 transients are similar for all 1CoCZ and 10CoCZ catalysts and appear independent of the
177 reduction temperature. Accordingly, we infer that the first step of CO_2 methanation, *i.e.*, CO_2
178 activation, is not structure-sensitive and does not depend on the extent of Co reduction.

179 Decomposition of formates can lead to the formation of carbonyl species³⁵. Consecutively,
180 adsorbed CO needs to dissociate to form methane. CO dissociation can be tracked by following
181 the oxidation state of cobalt by means of NEXAFS (near edge extended X-ray absorption fine
182 structure)³⁶ or synchrotron-based NAP-XPS (near-ambient pressure X-ray photoelectron
183 spectroscopy). However, such experiments are not feasible due to the low signal-to-noise ratio
184 for the samples with a low Co loading. Another approach to observe CO dissociation on CoCZ
185 catalysts is to determine the extent of oxygen spillover from cobalt to the CZ support¹⁴. Oxygen
186 formed during CO dissociation on a metal or at metal–oxide interfaces can re-oxidize Ce^{3+} via
187 oxygen spillover¹⁴. To probe this process, we performed resonant photoemission spectroscopy
188 (RPES) measurements, offering high sensitivity to changes in the Ce^{3+} concentration at the very
189 surface (**Fig. 3c, d, Supplementary Note 9**). Exposure of 10Co300 and 10Co500 samples to
190 CO at 50 °C led to the oxidation of both the CZ support and metallic Co nanoparticles (**Fig.**
191 **3e**). In contrast, exposure of the 1% CoCZ sample to CO did not result in Ce^{3+} oxidation. The
192 absence of CO dissociation for small fully reduced particles in 1Co500 is in line with literature
193 and follows conventional structure sensitivity³⁶. The absence of oxygen spillover for the
194 1Co300 sample indicates the inability of this catalyst to dissociate CO at 50 °C.

195 As CO dissociation over Co was demonstrated to be a hydrogen-assisted process³⁶, it strongly
196 depends on the ability of the catalyst to adsorb and dissociate hydrogen. To probe hydrogen
197 activation over the studied cobalt catalysts, we studied the hydrogenation of propylene with
198 parahydrogen. Pairwise insertion of parahydrogen into unsaturated molecules such as propylene
199 leads to parahydrogen-induced polarization (PHIP), which can be observed as an NMR signal
200 enhancement (SE) in the hydrogenated products³⁷. SE can be expected for supported metallic

201 nanoparticle catalysts when the mobility of hydrogen atoms on the metallic surface is hindered
202 by, for instance, carbonaceous deposits or when specific low-dimensional ensembles act as an
203 isolated active site for hydrogen activation. SE was also observed for single-atom active sites³⁸
204 and for catalysts following Eley–Rideal mechanism^{39,40}. Both 1CoCZ and 10CoCZ catalysts
205 reduced at 500 °C showed a high activity in propylene hydrogenation and an expectedly low
206 SE for propane (**Fig. 3h, Supplementary Note 10**). Although the CoCZ catalysts reduced at
207 300 °C were substantially less active in propylene hydrogenation, these samples displayed a
208 much higher SE than the fully reduced CoCZ samples. The highest SE of 70 was observed for
209 1Co300 (**Fig. 3f, h**). We explain the PHIP effect observed for 1Co300 by heterolytic
210 dissociation of hydrogen at the Co–CoO interface, although we cannot exclude that the Co–CZ
211 and CoO–CZ interfaces can also play a role. This interpretation is supported by the strong
212 irreversible adsorption of hydrogen (**Supplementary Note 10**) and the low H₂–D₂ exchange
213 rate (**Fig. 3g**) observed for the partially reduced CoCZ samples. Moreover, small fully reduced
214 cobalt particles (1Co500) showed a much higher reaction order with respect to H₂ for CH₄
215 formation than 1Co300, pointing to a low hydrogen coverage on the 1Co500 catalyst. These
216 findings evidence differences in hydrogen activation, which we expect to play a crucial role in
217 the unusual structure sensitivity trends of low-loaded CoCZ with respect to the reduction
218 temperature. Efficient hydrogen activation at the Co–CoO interface can have substantial
219 influence not only on CO₂ and CO activation, but also on the overall reaction mechanism of
220 CO₂ hydrogenation.

221

222 **Mechanistic differences metallic and interfacial sites**

223 Further insight into the mechanistic differences in CO₂ hydrogenation between CoCZ catalysts
224 was obtained with IR spectroscopy by following the transient behavior of formate and carbonyl
225 species upon isotope switching between ¹²CO₂/H₂ and ¹³CO₂/H₂ mixtures (**Fig. 4a, b,**
226 **Supplementary Note 11**). A first glance at the quantification of formate species for 1Co300
227 sample (**Fig. 4c**) suggests that their total residence time is much longer than that of adsorbed
228 CO. The formate transient can be deconvoluted in two contributions, namely a fast one assigned
229 to formates adsorbed on interfacial sites³¹ and a slow one due to formates on the support^{35,41}
230 (**Fig. 4b**). The initial rate of disappearance of the fast formates is higher than the one of
231 carbonyls (**Fig. 4c**, area marked with orange color), which indicates that the decomposition of
232 formate towards CO is faster than the hydrogenation of CO to methane. It has been earlier
233 reported that formate decomposition is the rate-determining step for CO formation³⁵. In order

234 to explore the influence of the reduction temperature on the formation/decomposition of
235 formates, we performed transient kinetic experiments with the 1CoCZ catalysts. **Fig. 4d** shows
236 the intensities of the formate IR signal during switches between H₂ and the CO₂+H₂ mixture.
237 Formates are rapidly formed on the 1Co300 sample, which presents the highest CO₂
238 hydrogenation activity. The formation of formates on 1Co500 is much slower. Moreover, the
239 large amount of accumulated formates under reaction conditions and slower hydrogenation of
240 the formates after a switch from CO₂/H₂ to H₂ as compared to the other samples points to the
241 poor hydrogenation activity of the 1Co500 sample. The high H₂-D₂ exchange activity,
242 reversible H₂ chemisorption, and low SE during the hydrogenation of propylene with
243 parahydrogen in combination with these IR results reflect the weak adsorption of hydrogen on
244 small metallic particles, which can explain the low activity of 1Co500 towards the
245 decomposition of formates and, henceforth, the low activity in CO₂ hydrogenation (**Fig. 4e**).
246 The dynamics of the formation and decomposition of formate species for 1Co275 were also
247 slower than for 1Co300, despite the strong H₂ adsorption on the former sample. Moreover, the
248 amount of formate species formed in 1Co275 is lower than in 1Co300. We speculate that strong
249 adsorption of hydrogen can impede CO₂ and formate hydrogenation, which is in line with the
250 low reaction orders with respect to H₂ in CO₂ hydrogenation. We also note the very low
251 intensity of the carbonyl band on 1Co275 and 1Co300 catalysts (**Fig. 4a, Supplementary Note**
252 **11**) under reaction conditions, which is consistent with a high H coverage. For the 10% CoCZ
253 catalysts containing larger metallic nanoparticles, the transient behavior with respect to the
254 formation/decomposition of formate species was similar to that of 1Co300. Moreover, a faster
255 initial rate of formate decomposition as compared to methanation of adsorbed CO was also
256 observed. However, IR spectra clearly show a much higher CO coverage for the catalysts that
257 contain large cobalt nanoparticles as compared to 1%CoCZ (**Supplementary Figure 71,**
258 **Supplementary Note 11**). The latter observation is in line with literature, reporting weak
259 adsorption of CO on small nanoparticles under reaction conditions⁸. The mechanistic insight
260 obtained by a combination of advanced *in situ* spectroscopy tools allowed us to explain the
261 unique activity of 1Co300 as compared to other CoCZ catalysts and to control CH₄ selectivity
262 in CO₂ hydrogenation (**Supplementary Note 5**).

263 **Conclusions**

264 Herein, we demonstrated the possibility to overcome classical structure sensitivity in CO₂
265 hydrogenation on cobalt catalysts by engineering metal-oxide interfaces. We used cobalt
266 loading and the reduction temperature as parameters governing the extent of metal-oxide

267 interfaces in CoCZ catalysts. Upon high-temperature reduction, catalysts display the size –
268 activity dependence typical for CO₂ hydrogenation, namely high activity only for large enough
269 cobalt nanoparticles. This structure-sensitivity limitation in terms of activity can be overcome
270 in turn by partial reduction of the cobalt particles at lower temperature, resulting in substantially
271 higher intrinsic activity. By use of advanced spectroscopic tools, we established that the active
272 phase in partially reduced 1Co300 catalyst consists of cobalt oxide covered with very small
273 metallic clusters of a few cobalt atoms. The CO₂ methanation reaction over these ensembles
274 follows the formate-mediated pathway. The outstanding catalytic activity at the metal–oxide
275 interface relates to the optimum adsorption/coverage of both reactants and intermediates,
276 heterolytic activation of hydrogen, hydrogen and oxygen spillover. The outlined approach will
277 be highly relevant to the design of more efficient catalysts for other structure-sensitive
278 reactions. For large-scale processes such as Fischer-Tropsch synthesis, methanol synthesis and
279 ammonia synthesis, higher activity and selectivity could be obtained by introducing appropriate
280 metal–metal oxide active sites. Moreover, the role of hydrogen activation in many of these
281 structure-sensitive hydrogenation reactions has not been fully recognized yet. For example, the
282 majority of studies in Fischer-Tropsch area are focused on the C–O bond activation and chain
283 growth reactions, while hydrogen adsorption and activation are usually not taken into account
284 as critical steps in the reaction mechanism.

285

286 **Methods**

287 ***Chemicals***

288 All chemicals were obtained from Sigma-Aldrich: cobalt acetate tetrahydrate, ammonium
289 hydroxide solution (25 %NH₃ in H₂O) and CeZrO₄ denoted as CZ (50/50 molar ratio)
290 nanopowder.

291 ***Preparation of CoCZ by strong electrostatic adsorption***

292 A series of CZ based catalysts with different metal loadings were prepared using a wet
293 impregnation method.¹⁴ For this purpose, the desired amount of cobalt acetate was dissolved in
294 50 ml of deionized water. The suspension obtained by adding 2 g of nanocrystalline CZ was
295 stirred for 2 hours. Then, the water was removed by evaporation. The catalysts were dried at
296 110 °C in air overnight and then calcined at 350 °C for 4 h. Prior to catalytic activity tests the
297 catalysts were reduced at 225 – 500 °C in H₂ for 4 h. The catalysts reduced at different
298 temperature are denoted as xCoy, where *x* is the Co loading and *y* the reduction temperature.

299 ***Sol-gel synthesis of single atom cobalt/ceria-zirconia (Co-doped CZ solid solution)***

300 In order to obtain a solid solution of cobalt-ceria-zirconia, a synthesis procedure reported by
301 Yuan et al⁴² was modified. In a typical synthesis, 0.8 g of Pluronic P123 (Sigma-Aldrich) and
302 the desired ratio of Ce(NO₃)₃·6H₂O (Sigma-Aldrich), ZrOCl₂·8H₂O (Sigma-Aldrich) and
303 Co(NO₃)₂·6H₂O (total amount of Co, Ce and Zr is 5 mmol) were added in 16 mL of ethanol.
304 After stirring for at least 2 h at room temperature, the homogeneous sol was transferred to an
305 oven at 40°C. After 48 h aging, the gel product was dried at 100°C for 24 h. Calcination was
306 carried out in air by slowly increasing the temperature from room temperature to 500 °C at a
307 rate of 1 °C min⁻¹, followed by a dwell of 4 h at 500 °C.

308 ***Cobalt nanoparticles supported on SiO₂***

309 Small cobalt nanoparticles were synthesized using wetness impregnation with cobalt
310 (tris)ethyleneamine precursor. The catalysts were dried at 110 °C in air overnight and then
311 pyrolyzed in helium flow at 350 °C for 4 h. Prior to catalytic activity tests, the catalysts were
312 reduced at 300 – 500 °C in H₂ for 4 h.

313 ***Characterization***

314 The characterization methods used in this work are largely the same as described in our previous
315 study of fully reduced cobalt in CoCZ catalysts.¹⁴

316 The crystalline structure of the catalysts was determined by recording X-ray diffraction (XRD)
317 patterns with a Bruker D2 Phaser diffractometer using Cu K α -radiation. The particle size was
318 estimated with the Scherrer equation. Reduced samples were transferred to the sample holder
319 via a glovebox. The samples were placed in an XRD sample holder and covered with Kapton
320 tape.

321 The metal content was determined using inductively coupled plasma optical emission
322 spectrometry (ICP-OES) with a Spectro CIROS CCD spectrometer. Prior to measurement, the
323 samples were dissolved in a 1:2.75 (by weight) mixture of (NH₄)₂SO₄ :(concentrated) H₂SO₄
324 and diluted with water.

325 Hydrogen temperature-programmed reduction (H₂-TPR) experiments were performed with a
326 Micromeritics Autochem II 2920 instrument. Typically, 100 mg catalyst was loaded in a tubular
327 quartz reactor. The sample was reduced in 4 vol% H₂ in N₂ at a flow rate of 50 mL/min, while
328 heating from room temperature up to 600 °C at a rate of 10 °C/min.

329 Transmission electron microscopy (TEM) images were acquired with a Tecnai 20 transmission
330 electron microscope (FEI, now Thermo Fisher Scientific) equipped with a LaB₆ filament and
331 operated at an acceleration voltage of 200 kV. Calcined catalysts were prepared by dropping a
332 suspension of finely ground material in analytical grade absolute ethanol onto Quantifoil R
333 1.2/1.3 holey carbon films supported on a Cu grid (200 mesh). TEM images were recorded on
334 a 4k x 4k CCD camera. Reduced catalysts were transferred to an Ar-filled glovebox and
335 dispersed in dry n-hexane, then a few droplets were placed on Cu TEM grids. The grid was
336 transported in a GATAN vacuum transfer holder (Model number CHVT3007, **Supplementary**
337 **Figure 1**).

338 The morphology and the nanoscale distribution of elements in the samples were studied using
339 scanning transmission electron microscopy - energy-dispersive x-ray spectroscopy (**STEM-**
340 **EDX**). Measurements were carried out on a FEI cubed Cs-corrected Titan operating at 300 kV.
341 Calcined samples were crushed, sonicated in ethanol and dispersed on a holey Cu support grid.

342 Reduced catalysts were passivated before sample preparation. Elemental analysis was done
343 with an Oxford Instruments EDX detector X-Max^N 100TLE.

344 Ex- and in situ Scanning Transmission electron microscopy – Electron energy loss spectroscopy
345 (STEM-EELS) measurements and ADF-STEM imaging were carried out using an aberration-
346 corrected ThermoFischer Scientific - Titan Cubed electron microscope, operating at 300 kV,
347 equipped with an energy monochromator. The monochromator was excited to a value of 1.2 to
348 achieve optimal energy resolution for EELS, giving us a FWHM value of 120 meV measured
349 at the zero-loss peak. A probe convergence semi-angle of 16 mrad was used. The gas and
350 heating cell holder (Climate G+, DENSsolutions) is made of two chips functionalized with
351 electron-transparent SiNx windows, forming a ‘nanoreactor’ inside the TEM column⁴³. The
352 thickness of the window membrane was approximately 50 nm (bottom window) + 30 nm (top
353 window). The temperature of the sample is accurately controlled via a 4-point probe method.
354 For the in-situ studies, the catalyst was reduced in the nanoreactor for 4 hours in a flow
355 consisting of 5 vol% H₂ in He and at temperatures of 300 °C and 500 °C. To minimize the effect
356 of the electron beam during the EELS line scans on the Co containing nanoparticles, the electron
357 dose was reduced by limiting the beam intensity. The measurements were performed at
358 atmospheric pressure.

359 CO and H₂ chemisorption measurements were carried out using a Micromeritics ASAP 2010C
360 instrument. Before each measurement, the samples were dried in vacuum at 110 °C. Samples
361 were subsequently heated in flowing H₂ with a rate of 10 °C/min to the final reduction
362 temperature of 275 – 500 °C. A reduction time of 4 h was used, after which the samples were
363 evacuated for 60 min at T + 20 °C. The CO adsorption isotherms were measured at 30 °C and
364 the H₂ adsorption isotherms were measured at 150 °C. The CO/Co and H₂/Co ratios at zero
365 pressure were determined by extrapolation of the linear part of the first isotherm. Particle size
366 estimations are based on the assumption of hemispherical geometry, assuming a CO/Co_s and
367 H/Co_s adsorption stoichiometry of 1.5 and 1, respectively (Co_s referring to metallic Co surface
368 sites).

369 X-ray photoelectron spectroscopy (XPS) was performed on a Thermo Scientific K-alpha
370 equipped with a monochromatic small-spot X-ray source and a 180° double focusing
371 hemispherical analyzer with a 128-channel detector. For a typical sample preparation, fresh
372 catalyst was pressed on carbon tape supported by an aluminium sample plate. Spectra were

373 recorded using an AlK α X-ray source (1486.6 eV, 72 W) and a spot size of 400 μm . Survey
374 scans were taken at a constant pass energy of 200, 0.5 eV step size, region scans at 50 eV
375 constant pass energy with a step size of 0.1 eV. The binding energies of the Co 2p and Ce 3d
376 regions were corrected to the U''' component of the Ce 3d line with a characteristic position of
377 916.7 eV^{44–46}.

378 *Quasi in situ X-ray photoelectron spectroscopy (XPS).*

379 Reduction of the CoCZ catalysts under mild conditions was studied by quasi in situ XPS using
380 a Kratos AXIS Ultra 600 spectrometer equipped with a monochromatic Al K α X-ray source (Al
381 K α energy 1486.6 eV). Survey and detailed region scans were recorded at pass energies of 160
382 eV and 40 eV, respectively, with a step size of 0.1 eV. The background pressure during the
383 measurements was lower than 5×10^{-6} mbar. A high-temperature reaction cell (Kratos, WX-
384 530) was used to pretreat the sample, which was supported on an alumina stub. This setup
385 allowed pretreatment in different gases and in vacuo sample transfer into the XPS measurement
386 chamber. Reduction was performed in a 10% H₂ in Ar flow (50 ml/min) at atmospheric pressure
387 and 300 °C for 4 h. After reduction the sample was cooled to 150 °C and subsequently
388 transferred to the measurement chamber. Energy calibration was done using the Ce 3d peak at
389 916.7 eV of the CeZrO₄ support, whose position is independent on reduction degree.

390 *Synchrotron-based near-ambient pressure X-ray photoelectron spectroscopy (NAP-XPS).*

391 Measurements were carried out on a commercial SPECS PHOIBOS 150 NAP energy analyzer
392 at the CIRCE beamline of the ALBA synchrotron light source. The CIRCE beamline is an
393 undulator beamline with 100 – 2000 eV photon energy range. XPS measurements at pressures
394 up to ~20 mbar are possible owing to a differential pumping system, which separates the
395 electron analyzer from the reaction area. The beam spot size at the sample was 100 x 65 μm^2 .
396 The angle between the sample normal and the photon beam was 75° and the angle between the
397 sample normal and the analyzer axes was 40°. The gas supply to the reaction chamber consisted
398 of calibrated mass-flow controllers, providing a total flow of 20 mL/min. The reaction pressure
399 was kept by using a primary pump directly connected to the analysis chamber and a manual
400 valve. All the gases used were of high purity (99.999%). The sample temperature was controlled
401 by using an infrared laser ($\lambda = 808$ nm) focused on a stainless steel plate, on top of which the
402 samples were mounted. The temperature was monitored during all the experiments with a K-
403 type thermocouple in direct contact with the samples. A standard residual gas analyzer (QMS)

404 located in the differential pumping stage of the analyzer allowed following the activity of the
405 catalyst treated in the reaction chamber during recording the XPS spectra. The total acquisition
406 time of the survey spectrum, O 1s, C 1s, Ce 3d, and Co 2p regions was around 60-70 min. A
407 pass energy of 10 eV was typically used for high resolution spectra (20 eV for survey) with a
408 step size of 0.1 eV and a dwell time of 0.5 s. The binding energies of the Co 2p and Ce 3d
409 regions were corrected to the U''' component of the Ce 3d line with a characteristic position of
410 916.7 eV⁴⁴⁻⁴⁶. The position and shape of this peak is independent of atomic ratio of Ce³⁺ to Ce⁴⁺
411 (as long as Ce⁴⁺ can be detected), allowing reliable energy calibration of the photoelectron
412 spectra at different reaction conditions. All the spectra are presented as recorded, meaning that
413 no normalization or other manipulations were performed.

414 *X-ray absorption near edge structure (XANES) spectroscopy.*

415 The oxidation state of the Co phase was studied during catalyst reduction using XANES.
416 Measurements were performed at the Co K-edge (7.7 keV) in transmission mode at beamline
417 B18 of the Diamond Light Source. The energy was selected with a Si(111) monochromator.
418 Energy calibration was performed using a Co foil ($E_0 = 7.709$ KeV). The photon flux of the
419 incoming and outgoing X-ray beam was determined using two ionization chambers. The
420 obtained X-ray absorption spectra were background-subtracted and normalized using Athena
421 software. Linear combination fitting of *operando* data was performed using three independently
422 recorded reference spectra of Co foil, CoO and Co₃O₄ powders. In a typical experiment, ca. 15
423 mg catalyst sample diluted with BN was placed in a tubular quartz reactor inside as described
424 elsewhere⁴⁷. Catalysts were reduced in this *operando* cell by heating at a rate of 10 °C/min to
425 550 °C followed by an isothermal dwell of 20 min in a flow of 10 vol% H₂ in He at a total flow
426 rate of 50 mL/min.

427 *Fourier-transform infrared spectroscopy (FTIR).*

428 Infrared spectra were recorded on a Bruker Vertex 70v FTIR spectrometer equipped with a
429 DTGS detector. The experiments were performed in situ by using a home-built environmental
430 transmission IR cell. Self-supporting pellets were made by pressing approximately 12 mg of a
431 sample in a disk with a diameter of 13 mm. Each spectrum was collected by averaging 64 scans
432 with a resolution of 2 cm⁻¹ in the 4000-1000 cm⁻¹ range. The samples were reduced in a 10 %
433 H₂/He mixture at different temperatures in the 275 – 500 °C range for 4 h after heating at a rate

434 of 10 °C/min. For all samples background was subtracted and intensity was normalized to the
435 weight of the pellet.

436 *CO adsorption at 50 °C.*

437 For CO adsorption experiments the samples were outgassed at T + 20 °C prior cooling in
438 vacuum to 50 °C. IR spectra were recorded as a function of CO partial pressure in the 0 – 10
439 mbar range.

440 *CO adsorption at liquid nitrogen temperature.*

441 For CO adsorption experiments the samples were outgassed at T + 20 °C prior cooling down in
442 vacuum to 50 °C. IR spectra were recorded as a function of CO partial pressure in the 0 – 10
443 mbar range.

444 *Operando FTIR.*

445 For the steady-state measurements, the samples after reduction were cooled down in 10 %
446 H₂/He mixture to the reaction temperature prior exposure to 2.5% CO₂/10% H₂/87.5 % He
447 mixture (total flow of 200 ml/min). For transient experiments, after reduction the samples were
448 exposed to different gas mixtures H₂/He, ¹²CO₂/He, ¹²CO₂/H₂/He and ¹³CO₂/H₂/He, while
449 recording IR spectra every 0.8 s or 15 s. For all samples, the background was subtracted and
450 intensity was normalized to the weight of the pellet.

451 *Propylene hydrogenation with para-hydrogen (p-H₂).*

452 The reaction was carried out in a 1/4" OD stainless-steel reactor in which 50 mg of CoCZ
453 catalyst (sieve fraction 125–250 μm) was placed between two pieces of fiberglass tissue
454 (**Supplementary Figure 2**). The reactor was heated with a tube furnace. Prior to reaction
455 experiments, the catalysts were reduced at 300 °C or 500 °C in a flow of 5 vol% H₂ in Ar for 4
456 h (30 ml/min). The reaction feed for propylene hydrogenation consisted of propylene and
457 hydrogen in a 1:4 ratio. Hydrogen was enriched in parahydrogen up to 85% using a Bruker
458 Parahydrogen Generator BPHG-90. The gas flow rate was controlled using an Aalborg
459 rotameter and was frequently interrupted in order to acquire stopped-flow spectra for

460 conversion calculation. The reactor effluent was led through a NMR tube placed inside the
461 NMR spectrometer. The samples were characterized in ALTADENA (adiabatic longitudinal
462 transport after dissociation engenders net alignment) conditions⁴⁸, where the reaction is
463 conducted in the Earth's magnetic field and the reaction products are subsequently transferred
464 into the NMR spectrometer for detection. ¹H NMR spectra were acquired on a 300 MHz Bruker
465 AV 300 NMR spectrometer using a $\pi/2$ rf pulse. All experiments were performed at
466 atmospheric pressure. The NMR signal enhancement factor (*SE*) is calculated as the ratio
467 between the integral of the signal of hyperpolarized propylene and the integral of the
468 corresponding signal of thermally polarized propylene.

469 *H₂ – D₂ exchange.*

470 Experiments were performed to evaluate the ability of the catalyst to active hydrogen. We
471 compared the performance of 1% CoCZ and 10% CoCZ with a bare CZ support. After
472 reduction, the samples were cooled to 200 °C and exposed to a mixture of H₂/D₂/Ar (1:1:48, 50
473 mL/min). The signals of hydrogen (*m/z* = 2), deuterium (*m/z* = 4), and HD (*m/z* = 3) were
474 monitored online using mass spectrometry. The TOF of HD formation was determined by
475 normalizing the rate to the amount of metallic cobalt sites obtained from CO chemisorption.

476 *CO₂ hydrogenation.*

477 Measurements were performed in a 10-tube parallel microflow reactor. The samples were
478 pressed, sieved and crushed and the fraction between 125 μm and 250 μm was used. Each quartz
479 reactor was filled with 50 mg of sample diluted with 200 mg of SiC of the same sieve fraction.
480 The obtained mixture was enclosed between two quartz wool plugs. The reaction was
481 performed at atmospheric pressure. Prior to reaction, the catalysts were reduced *in situ* in a flow
482 consisting of 10 vol% H₂ in He (total flow rate 50 mL/min STP per reactor tube), whilst heating
483 from room temperature to 500 °C at a rate of 10 °C/min, followed by an isothermal dwell of
484 4 h. After cooling to reaction temperature in the same flow, the pre-treatment gas was replaced
485 by a feed consisting of 5 vol% CO₂ and 20 vol% H₂ in He (total flow rate 50 mL/min STP). The
486 temperature was increased by steps of 25 °C at a rate of 5 °C/min. When the target temperature
487 was reached, a period of 20 min was allowed for stabilization. Then, the effluent gas was
488 analyzed by online gas chromatography with an Interscience Compact GC equipped with Plot
489 (TCD) and Molsieve (TCD) columns.

490 ***Density functional theory calculations.***

491 Spin-polarized DFT calculations were performed with the Vienna Ab Initio Simulation
492 Package^{49,50}. The projector-augmented wave (PAW) method was used to describe the electron-
493 ion interactions⁵¹. To account for the effect of the exchange–correlation and on-site Coulomb
494 interaction, the Perdew–Burke–Ernzerhof (PBE) functional⁵² with the Hubbard + U correction
495 was used. Here, U = 4.1 eV for Co was chosen based on previous studies⁵³. The cut-off energy
496 for the plane-wave basis set was 400 eV. The geometry optimizations were assumed converged
497 when the Hellmann-Feynman forces acting on atoms were less than 0.05 eV/Å. For the cobalt
498 oxide support, we constructed a CoO(111) slab model with 4×4 unit cell and six atomic layers.
499 The top three layers were relaxed and the bottom three layers were frozen to the configuration
500 of the bulk. To mimick a large cobalt nanoparticle on the support, the stable Co(111) surface
501 with 3×3 unit cell and four atomic layers was constructed. The top two layers were relaxed and
502 the bottom two layers were frozen. To study the catalytic properties of cobalt oxide supported
503 single atom or cobalt clusters, we considered as structural models a single Co atom (Co₁) and
504 Co clusters with 4 (Co₄), 6 (Co₆) and 8 (Co₈) Co atoms supported on CoO(111). A vacuum
505 thickness of 15 Å was used to avoid spurious interactions of adsorbates between neighbouring
506 super cells. For the Brillouin zone integration, a 3×3×1 Monkhorst-Pack *k*-point was adopted
507 for the above unit cells. Vibrational stretching frequencies of adsorbed CO were computed
508 using a mass-weighted normal mode analysis under the harmonic approximation. The forces
509 obtained from VASP calculations were used to construct the relevant Hessians matrix. The
510 vibrational frequencies were extracted from these matrices as eigenvalues.

511

512 **Data availability**

513 All data is available from the authors upon reasonable request. Coordinates of optimized
514 structures used for DFT modeling are contained in Supplementary Data 1.

515

516 **References**

- 517 1. Yang, X. F. *et al.* Single-atom catalysts: A new frontier in heterogeneous catalysis.
518 *Acc. Chem. Res.* **46**, (2013).
- 519 2. Liu, L. & Corma, A. Metal catalysts for heterogeneous catalysis: From single atoms to
520 nanoclusters and nanoparticles. *Chemical Reviews* **118**, 4981–5079 (2018).
- 521 3. Somorjal, G. A. & Carrazza, J. Structure sensitivity of catalytic reactions. *Ind. Eng.*
522 *Chem. Fundam.* **25**, 63–69 (1986).
- 523 4. Van Santen, R. A. Complementary structure sensitive and insensitive catalytic
524 relationships. *Acc. Chem. Res.* **42**, 57–66 (2009).
- 525 5. Honkala, K. *et al.* Ammonia synthesis from first-principles calculations. *Science* **307**,
526 555–558 (2005).
- 527 6. Dahl, S. *et al.* Role of steps in N₂ activation on Ru(0001). *Phys. Rev. Lett.* **83**, 1814–
528 1817 (1999).
- 529 7. Bezemer, G. L. *et al.* Cobalt particle size effects in the Fischer-Tropsch reaction
530 studied with carbon nanofiber supported catalysts. *J. Am. Chem. Soc.* **128**, 3956–3964
531 (2006).
- 532 8. Vogt, C. *et al.* Unravelling structure sensitivity in CO₂ hydrogenation over nickel. *Nat.*
533 *Catal.* **1**, 127–134 (2018).
- 534 9. van den Berg, R. *et al.* Structure sensitivity of Cu and CuZn catalysts relevant to
535 industrial methanol synthesis. *Nat. Commun.* **7**, 13057 (2016).
- 536 10. Crampton, A. S. *et al.* Structure sensitivity in the nonscalable regime explored via
537 catalysed ethylene hydrogenation on supported platinum nanoclusters. *Nat. Commun.*
538 **7**, 1–12 (2016).
- 539 11. Vogt, C., Kranenborg, J., Monai, M. & Weckhuysen, B. M. Structure sensitivity in
540 steam and dry methane reforming over nickel: activity and carbon formation. *ACS*
541 *Catal.* **10**, 1428–1438 (2020).
- 542 12. Vogt, C., Monai, M., Kramer, G. J. & Weckhuysen, B. M. The renaissance of the
543 Sabatier reaction and its applications on Earth and in space. *Nat. Catal.* **2**, 188–197
544 (2019).
- 545 13. den Breejen, J. P. *et al.* On the origin of the cobalt particle size effects in
546 Fischer–Tropsch catalysis. *J. Am. Chem. Soc.* **131**, 7197–7203 (2009).
- 547 14. Parastaev, A. *et al.* Boosting CO₂ hydrogenation via size-dependent metal–support
548 interactions in cobalt/ceria-based catalysts. *Nat. Catal.* **3**, 526–533 (2020).
- 549 15. Cargnello, M. *et al.* Control of metal nanocrystal size reveals metal-support interface
550 role for ceria catalysts. *Science* **341**, 771–773 (2013).
- 551 16. Ye, T. N. *et al.* Vacancy-enabled N₂ activation for ammonia synthesis on an Ni-loaded
552 catalyst. *Nature* **583**, 391–395 (2020).
- 553 17. Qiao, B. *et al.* Single-atom catalysis of CO oxidation using Pt₁/FeO_x. *Nat. Chem.* **3**,
554 634–641 (2011).

- 555 18. Fu, Q., Saltsburg, H. & Flytzani-Stephanopoulos, M. Active nonmetallic Au and Pt
556 species on ceria-based water-gas shift catalysts. *Science* **301**, 935–938 (2003).
- 557 19. Zhai, Y. *et al.* Alkali-stabilized Pt-OH_x species catalyze low-temperature water-gas
558 shift reactions. *Science* **329**, 1633–1636 (2010).
- 559 20. Melaet, G. *et al.* Evidence of highly active cobalt oxide catalyst for the Fischer-
560 Tropsch synthesis and CO₂ hydrogenation. *J. Am. Chem. Soc.* **136**, 2260–2263 (2014).
- 561 21. Zhao, K. *et al.* Unraveling and optimizing the metal-metal oxide synergistic effect in a
562 highly active Co_x(CoO)_{1-x} catalyst for CO₂ hydrogenation. *J. Energy Chem.* **53**, 241–
563 250 (2020).
- 564 22. Have, I. C. te. *et al.* Uncovering the reaction mechanism behind CoO as active phase
565 for CO₂ hydrogenation. *Nat. Commun.* **2022 131 13**, 1–11 (2022).
- 566 23. Shin, H. K., Nam, I. S., Lee, J. S., Chung, J. S. & Moon, S. H. Catalytic properties of
567 partially reduced cobalt wire in CO hydrogenation. *Korean J. Chem. Eng.* **1996 131 13**,
568 54–59 (1996).
- 569 24. Ra, E. C. *et al.* Recycling carbon dioxide through catalytic hydrogenation: Recent key
570 developments and perspectives. *ACS Catal.* **10**, 11318–11345 (2020).
- 571 25. Tang, H. *et al.* Classical strong metal–support interactions between gold nanoparticles
572 and titanium dioxide. *Sci. Adv.* **3**, e1700231 (2017).
- 573 26. Matsubu, J. C., Yang, V. N. & Christopher, P. Isolated metal active site concentration
574 and stability control catalytic CO₂ reduction selectivity. *J. Am. Chem. Soc.* **137**, 3076–
575 3084 (2015).
- 576 27. Cao, S. *et al.* High-loading single Pt atom sites [Pt-O(OH)_x] catalyze the CO PROX
577 reaction with high activity and selectivity at mild conditions. *Sci. Adv.* **6**, 3809–3826
578 (2020).
- 579 28. DeRita, L. *et al.* Catalyst Architecture for Stable Single Atom Dispersion Enables Site-
580 Specific Spectroscopic and Reactivity Measurements of CO Adsorbed to Pt Atoms,
581 Oxidized Pt Clusters, and Metallic Pt Clusters on TiO₂. *J. Am. Chem. Soc.* **139**, 14150–
582 14165 (2017).
- 583 29. Weststrate, C. J., van de Loosdrecht, J. & Niemantsverdriet, J. W. Spectroscopic
584 insights into cobalt-catalyzed Fischer-Tropsch synthesis: A review of the carbon
585 monoxide interaction with single crystalline surfaces of cobalt. *J. Catal.* **342**, 1–16
586 (2016).
- 587 30. Wang, F. *et al.* Active Site Dependent Reaction Mechanism over Ru/CeO₂ Catalyst
588 toward CO₂ Methanation. *J. Am. Chem. Soc.* **138**, 6298–6305 (2016).
- 589 31. Aldana, P. A. U. *et al.* Catalytic CO₂ valorization into CH₄ on Ni-based ceria-zirconia.
590 Reaction mechanism by operando IR spectroscopy. *Catal. Today* **215**, 201–207 (2013).
- 591 32. Lin, S. S.-Y., Daimon, H. & Ha, S. Y. Co/CeO₂-ZrO₂ catalysts prepared by
592 impregnation and coprecipitation for ethanol steam reforming. *Appl. Catal. A Gen.* **366**,
593 252–261 (2009).
- 594 33. Vayssilov, G. N., Mihaylov, M., Petkov, P. S., Hadjiivanov, K. I. & Neyman, K. M.
595 Reassignment of the vibrational spectra of carbonates, formates, and related surface
596 species on ceria: A combined density functional and infrared spectroscopy

- 597 investigation. *J. Phys. Chem. C* **115**, 23435–23454 (2011).
- 598 34. Daturi, M. *et al.* Study of bulk and surface reduction by hydrogen of $Ce_xZr_{1-x}O_2$
599 mixed oxides followed by FTIR spectroscopy and magnetic balance. *J. Phys. Chem. B*
600 **103**, 4884–4891 (1999).
- 601 35. Wang, X., Shi, H. & Szanyi, J. Controlling selectivities in CO_2 reduction through
602 mechanistic understanding. *Nat. Commun.* **8**, 513 (2017).
- 603 36. Tuxen, A. *et al.* Size-dependent dissociation of carbon monoxide on cobalt
604 nanoparticles. *J. Am. Chem. Soc.* **135**, 2273–2278 (2013).
- 605 37. Bowers, C. R. & Weitekamp, D. P. Parahydrogen and synthesis allow dramatically
606 enhanced nuclear alignment. *J. Am. Chem. Soc.* **109**, 5541–5542 (1987).
- 607 38. Corma, A., Salnikov, O. G., Barskiy, D. A., Kovtunov, K. V & Koptuyug, I. V. Single-
608 atom gold catalysis in the context of developments in parahydrogen-induced
609 polarization. *Chem. – A Eur. J.* **21**, 7012–7015 (2015).
- 610 39. Pokochueva, E. V., Burueva, D. B., Salnikov, O. G. & Koptuyug, I. V. Heterogeneous
611 catalysis and parahydrogen-induced polarization. *ChemPhysChem* **22**, 1421–1440
612 (2021).
- 613 40. Kovtunov, K. V. *et al.* Catalytic hydrogenation with parahydrogen: a bridge from
614 homogeneous to heterogeneous catalysis. *Pure Appl. Chem.* **92**, 1029–1046 (2020).
- 615 41. Galhardo, T. S. *et al.* Optimizing Active Sites for High CO Selectivity during CO_2
616 Hydrogenation over Supported Nickel Catalysts. *J. Am. Chem. Soc.* **143**, 4268–4280
617 (2021).
- 618 42. Yuan, Q. *et al.* Ordered Mesoporous $Ce_{1-x}Zr_xO_2$ Solid Solutions with Crystalline
619 Walls. *J. AM. CHEM. SOC* **129**, 6698–6699 (2007).
- 620 43. Altantzis, T. *et al.* Three-Dimensional Quantification of the Facet Evolution of Pt
621 Nanoparticles in a Variable Gaseous Environment. *Nano Lett.* **19**, 477–481 (2018).
- 622 44. Artiglia, L. *et al.* Introducing Time Resolution to Detect Ce^{3+} Catalytically Active
623 Sites at the Pt/ CeO_2 Interface through Ambient Pressure X-ray Photoelectron
624 Spectroscopy. *J. Phys. Chem. Lett.* **8**, 102–108 (2017).
- 625 45. Skála, T., Šutara, F., Prince, K. C. & Matolín, V. Cerium oxide stoichiometry alteration
626 via Sn deposition: Influence of temperature. *J. Electron Spectros. Relat. Phenomena*
627 **169**, 20–25 (2009).
- 628 46. Stadnichenko, A. I. *et al.* Study of active surface centers of Pt/ CeO_2 catalysts prepared
629 using radio-frequency plasma sputtering technique. *Surf. Sci.* **679**, 273–283 (2019).
- 630 47. Kosinov, N. *et al.* Confined Carbon Mediating Dehydroaromatization of Methane over
631 Mo/ZSM-5. *Angew. Chemie - Int. Ed.* **57**, 1016–1020 (2018).
- 632 48. Pravica, M. G. & Weitekamp, D. P. Net NMR alignment by adiabatic transport of
633 parahydrogen addition products to high magnetic field. *Chem. Phys. Lett.* **145**, 255–258
634 (1988).
- 635 49. Kresse, G. & Furthmüller, J. Efficient iterative schemes for *ab initio* total-energy
636 calculations using a plane-wave basis set. *Phys. Rev. B* **54**, 11169 (1996).

- 637 50. Kresse, G. & Hafner, J. *Ab initio* molecular dynamics for liquid metals. *Phys. Rev. B*
638 **47**, 558 (1993).
- 639 51. Blöchl, P. E. Projector augmented-wave method. *Phys. Rev. B* **50**, 17953 (1994).
- 640 52. Perdew, J. P., Burke, K. & Ernzerhof, M. Generalized Gradient Approximation Made
641 Simple. *Phys. Rev. Lett.* **77**, 3865 (1996).
- 642 53. Park, K. W. & Kolpak, A. M. Understanding photocatalytic overall water splitting on
643 CoO nanoparticles: Effects of facets, surface stoichiometry, and the CoO/water
644 interface. *J. Catal.* **365**, 115–124 (2018).

645

646 **Fig. 1. The influence of catalyst reduction temperature on structure sensitivity in CO₂**
647 **methanation. a,** Catalytic activity of CoCZ catalysts reduced at different temperatures in CO₂
648 methanation at 250 °C normalized to the total metal amount (5 % CO₂/20 % H₂ balanced with
649 He, total flow 50 ml/min, 50 mg of sample). Red dashed line represents conventional volcano
650 plot with an optimum around 7 – 9 nm linked to classical structure sensitivity observed for
651 cobalt nanoparticles, orange line represents unconventional volcano plot with an optimum at
652 reduction temperature of 300 °C. STEM energy dispersive X-ray (STEM-EDX) maps of as-
653 prepared 1% CoCZ (b) and 10% CoCZ (c) samples in vacuum. d, Annular dark field STEM
654 (ADF-STEM) image of 1Co500 obtained in 5 % H₂/He at 500 °C after reduction for 4 h. Inset:
655 EELS spectra of 1Co500 obtained during line scan (Co surface – Co bulk – Co surface) in 5 %
656 H₂/He at 500 °C.

657 **Fig. 2. Nature of the active sites. a,** Quasi in situ XPS spectrum of 1Co300 obtained in vacuum
658 after reduction for 4 h in 50 mbar H₂ (hν = 1486 eV). b, Synchrotron-NAP-XPS spectrum of
659 1Co300 obtained in 1 mbar H₂ at 300 °C after reduction for 4 h in 10 mbar H₂ (hν = 1050 eV).
660 c, IR spectra of CO adsorbed on 1Co300 sample obtained at –170 °C. d, CO adsorption IR
661 spectra at 50 °C obtained for 1 % CoCZ sample reduced at 275 °C, 300 °C, 350 °C and 500
662 °C. e, Frequency of linearly adsorbed carbonyls as a function of CO partial pressure.
663 Schematic representation of the small (f) and large (g) Co NPs obtained after mild reduction
664 at 300 °C (blue – CoO, black Co⁰ clusters and islands).

665 **Fig. 3. Structure sensitivity of CO₂, CO and H₂ activation. a,** Background-subtracted spectra
666 obtained by operando IR at 250 °C in reaction mixture (CO₂ 2.5%, H₂ 10 %, He 87.5%, total
667 flow of 200 ml/min) for 1% and 10% CoCZ catalysts reduced at 300 °C and 500 °C. b, Transient
668 CO₂ hydrogenation experiments (switches from H₂ to a CO₂+H₂ mixture, then H₂ at 250 °C)
669 followed by IR spectroscopy: position of the hydroxyl species and IR intensity of the 2115 cm⁻¹
670 (normalized to the intensity of 2115 cm⁻¹ band of reduced sample). Resonant photoelectron
671 spectroscopy (RPES) data of Ce 4d-4f transitions for 1Co300 and 10Co300 as a function of
672 reaction atmosphere at 50 °C: (c) 1 mbar H₂; (d) 1 mbar CO. Blue line corresponds to spectra
673 taken at 124 eV, red at 120 eV and grey at 114 eV. e, Ce oxidation state for 1% CoCZ and 10%
674 CoCZ reduced at 300 °C and 500 °C before and after exposure to 1 mbar CO at 50 °C. f, ¹H
675 NMR spectrum acquired during hydrogenation of propylene with parahydrogen over 1Co300
676 at 250 °C and the gas flow of 3.8 mL/s (green) and stopped-flow spectrum acquired for
677 conversion calculation (blue). g, turnover frequency (TOF) for H₂ – D₂ exchange at 200 °C as

678 a function of the reduction temperature for the 1% and 10% CoCZ samples ($H_2/D_2/Ar=1/1/48$,
679 total flow 50 mL/min, 3 mg of 10% CoCZ and 10 mg of 1% CoCZ); **h**, 1H NMR signal
680 enhancements of propane during hydrogenation of propylene with parahydrogen at 250 °C
681 over 1% CoCZ and 10% CoCZ samples reduced at 300 °C and 500 °C.

682 **Fig. 4. CO₂ hydrogenation mechanism probed by transient IR spectroscopy.** Contour maps of
683 carbonyl (**a**) and formate (**b**) regions of IR spectra obtained for 1Co300 catalyst after the
684 $^{12}CO_2/H_2/He \rightarrow ^{13}CO_2/H_2/He$ switch at 200 °C (time resolution 0.8 s). **c**, Normalized response
685 of CO₂ and carbonyl and formate species. **d**, Formation and decomposition of formate species
686 for 1% CoCZ catalysts reduced at 275, 300 and 500 °C during $H_2 \rightarrow H_2 + CO_2 \rightarrow H_2$ switches
687 at 300 °C (time resolution 15 s). **e**, schematic representation of the surface species for 1Co300
688 and 1Co500 catalysts.

689

690 **Acknowledgments**

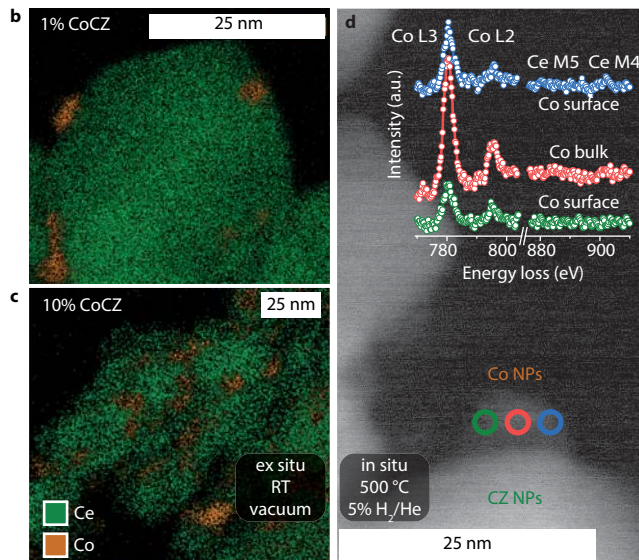
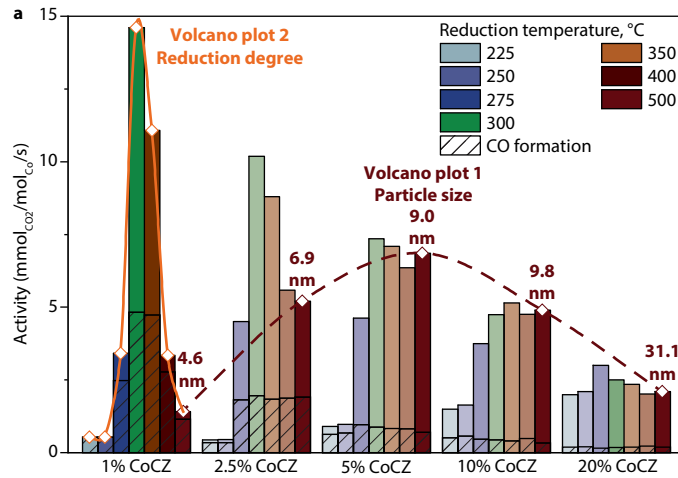
691 This research was supported by the Applied and Engineering Sciences division of the
692 Netherlands Organization for Scientific Research through the Alliander (now Qirion)
693 Perspective program on Plasma Conversion of CO₂. We acknowledge Diamond Light Source
694 for time on beamline B18 under proposal SP20715-1. This project has received funding from
695 the European Union's Horizon 2020 research and innovation programme under grant agreement
696 No 823717 – ESTEEM3. S.B. acknowledges support from the European Research Council
697 (ERC Consolidator Grant #815128 REALNANO) and T.A. acknowledges funding from the
698 University of Antwerp Research fund (BOF). A.B. received funding from the European Union
699 under grant agreement No 823717 – ESTEEM3. The authors acknowledge funding through the
700 Hercules grant (FWO, University of Antwerp) I003218N "Infrastructure for imaging nanoscale
701 processes in gas/vapour or liquid environments". I.V.K., D.B.B., and E.V.P. acknowledge the
702 Russian Ministry of Science and Higher Education (contract 075-15-2021-580) for financial
703 support of parahydrogen-based studies. Experiments using synchrotron radiation XPS were
704 performed at the CIRCE beamline at ALBA Synchrotron with the collaboration of ALBA staff.
705 F. Oropeza Palacio and Rim C.J. van de Poll are acknowledged for the help with RPES
706 measurements.

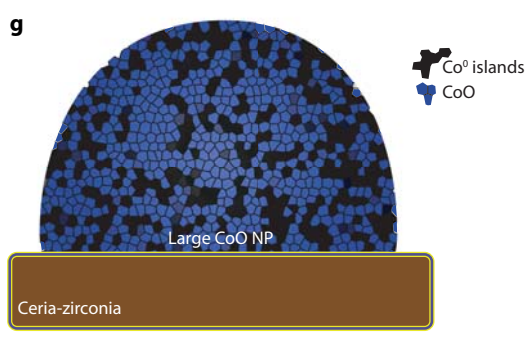
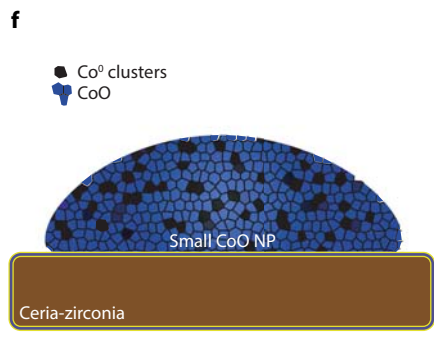
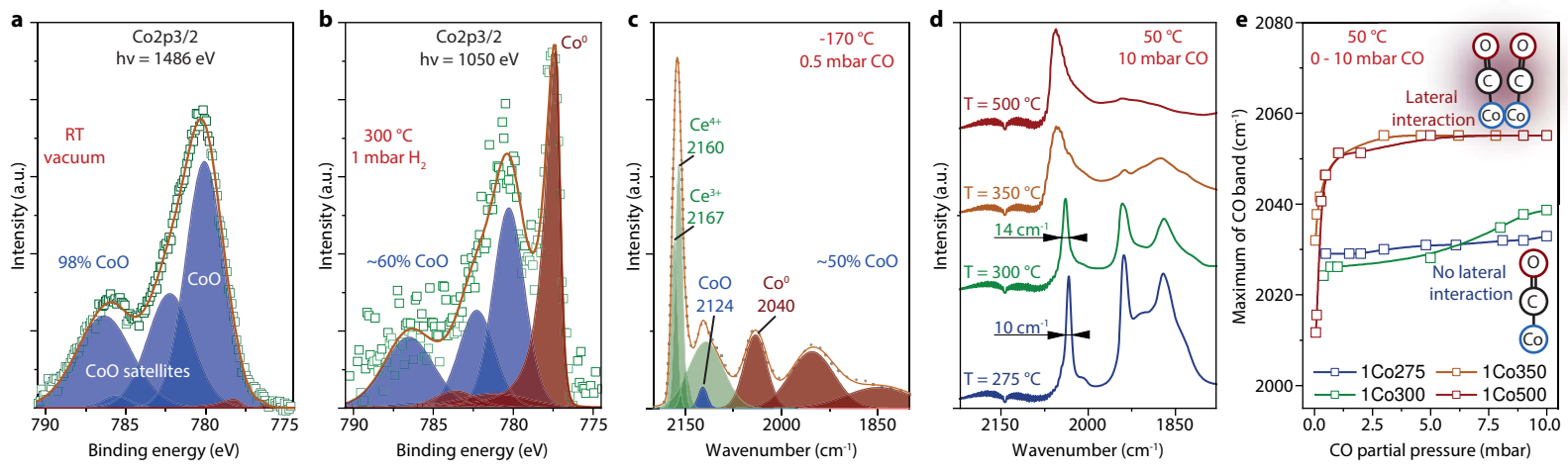
707 **Author contributions**

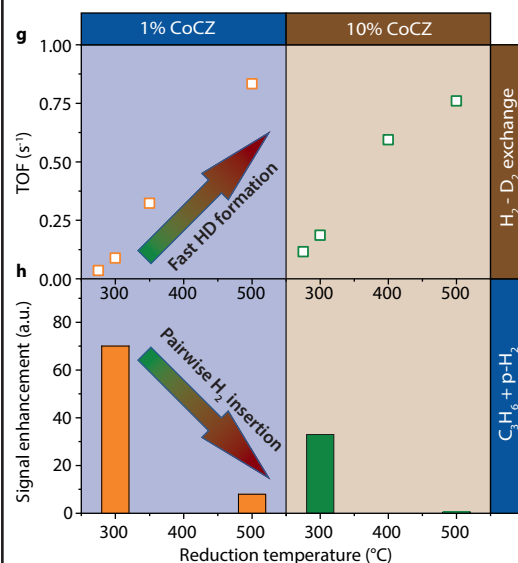
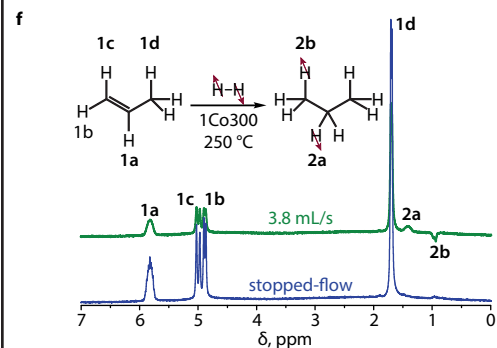
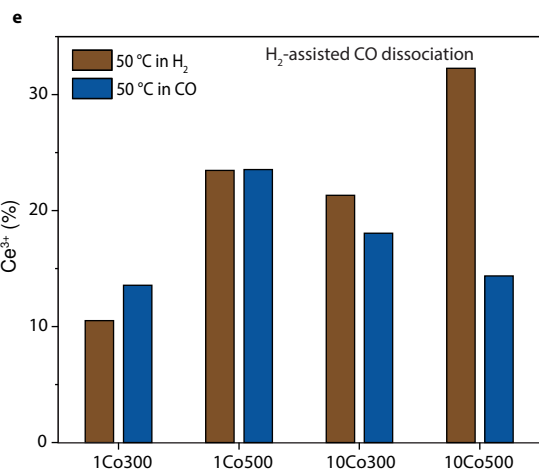
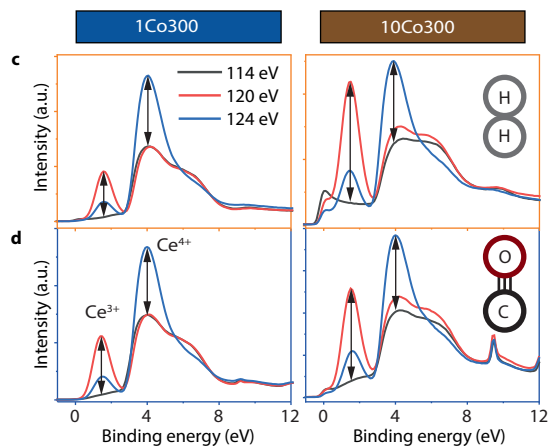
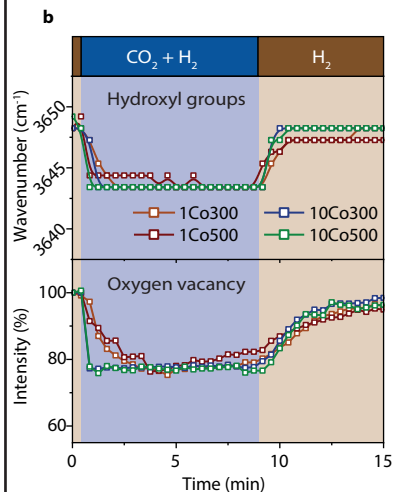
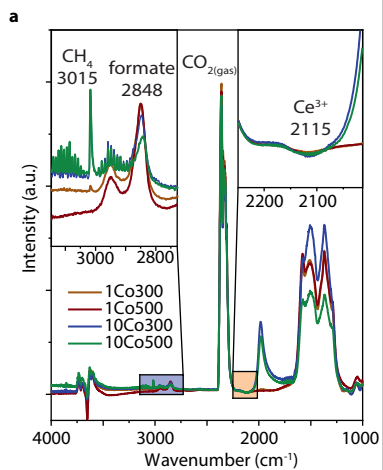
708 A.P. synthesized and characterized the set of ceria-zirconia samples (TPR, XRD and CO
709 chemisorption and IR spectroscopy). A.P. and E.H.O. performed the catalytic measurements.
710 V.M., A.P. and N.K. performed the *in situ* NAP-XPS and operando XAS measurements and
711 interpreted the results. A.J.F.H. performed TEM measurements with an *in situ* holder. T.F.K.
712 performed *quasi in situ* XPS. J.F.M.S. and J.J.C.S. wrote MATLAB script for rapid-scan FTIR
713 measurements. A.P. and E.U. performed H₂ – D₂ exchange experiments. I.V.K., D.B.B., and
714 E.V.P. performed and interpreted experiments with parahydrogen. T.A., P.L., A.B., S.B., A.P.
715 and N.K. performed and interpreted the *in situ* STEM-EELS experiments. A.P., V.M., N.K. and
716 E.J.M.H. wrote the paper. All authors discussed the results and commented on the manuscript.

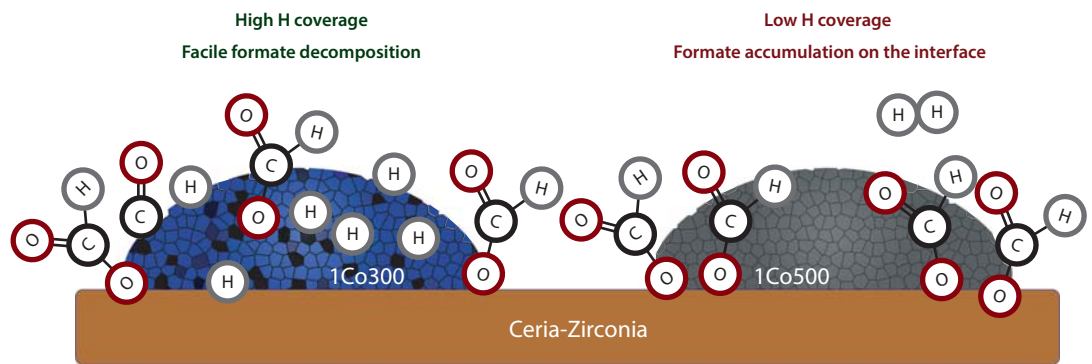
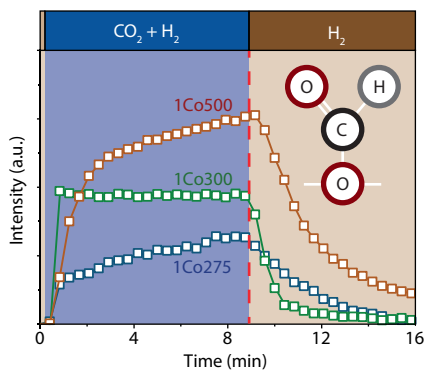
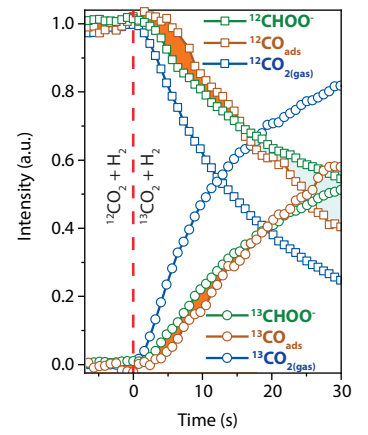
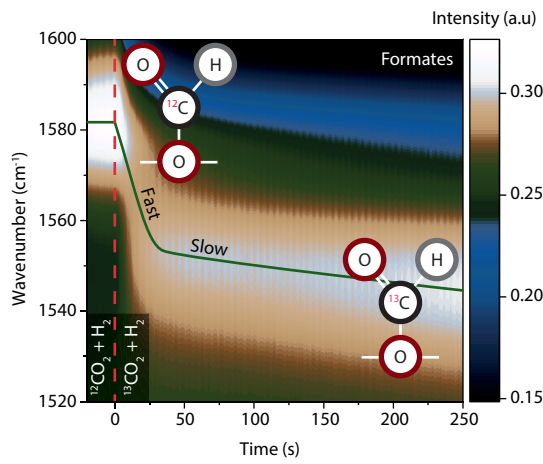
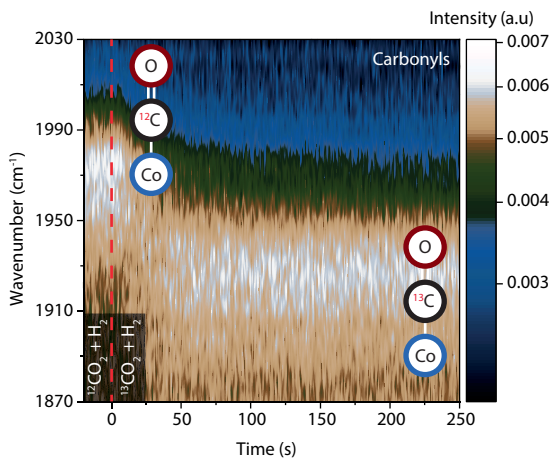
717 **Competing interests**

718 The authors declare no competing interests.









CO₂ conversion rate

